8-14-2018

Multi-Beam Scan Analysis with a Clinical LINAC for High Resolution Cherenkov-Excited Molecular Luminescence Imaging in Tissue.

Mengyu Jeremy Jia
Dartmouth College

Peter Bruza
Dartmouth College

Lesley A. Jarvis
Dartmouth College

David J. Gladstone
Dartmouth College

Brian W. Pogue
Dartmouth College

Research Article | Vol. 9, No. 9 | 1 Sep 2018 | BIOMEDICAL OPTICS EXPRESS 4217
Biomedical Optics EXPRESS

Multi-beam scan analysis with a clinical LINAC for high resolution Cherenkov-excited molecular luminescence imaging in tissue

MENGYU JEREMY JIA,[1,*] PETR BRUZA,[1] LESLEY A. JARVIS,[3] DAVID J. GLADSTONE,[1,2,3] AND BRIAN W. POGUE[1,2]

[1]*Thayer School of Engineering, Dartmouth College, Hanover, NH 03755, USA*
[2]*Norris Cotton Center, Dartmouth-Hitchcock Medical Center, Lebanon, NH 03756, USA*
[3]*Department of Medicine, Geisel School of Medicine, Dartmouth College, Hanover, NH 03755, USA*
**Mengyu.jia@dartmouth.edu*

Abstract: Cherenkov-excited luminescence scanned imaging (CELSI) is achieved with external beam radiotherapy to map out molecular luminescence intensity or lifetime in tissue. Just as in fluorescence microscopy, the choice of excitation geometry can affect the imaging time, spatial resolution and contrast recovered. In this study, the use of spatially patterned illumination was systematically studied comparing scan shapes, starting with line scan and block patterns and increasing from single beams to multiple parallel beams and then to clinically used treatment plans for radiation therapy. The image recovery was improved by a spatial-temporal modulation-demodulation method, which used the ability to capture simultaneous images of the excitation Cherenkov beam shape to deconvolve the CELSI images. Experimental studies used the multi-leaf collimator on a clinical linear accelerator (LINAC) to create the scanning patterns, and image resolution and contrast recovery were tested at different depths of tissue phantom material. As hypothesized, the smallest illumination squares achieved optimal resolution, but at the cost of lower signal and slower imaging time. Having larger excitation blocks provided superior signal but at the cost of increased radiation dose and lower resolution. Increasing the scan beams to multiple block patterns improved the performance in terms of image fidelity, lower radiation dose and faster acquisition. The spatial resolution was mostly dependent upon pixel area with an optimized side length near 38mm and a beam scan pitch of $P = 0.33$, and the achievable imaging depth was increased from 14mm to 18mm with sufficient resolving power for 1mm sized test objects. As a proof-of-concept, *in-vivo* tumor mouse imaging was performed to show 3D rendering and quantification of tissue pO_2 with values of 5.6mmHg in a tumor and 77mmHg in normal tissue.

OCIS codes: (170.3010) Image reconstruction techniques; (170.3880) Medical and biological imaging; (170.7440) X-ray imaging; (170.6920) Time-resolved imaging; (260.3800) Luminescence.

References and links

1. R. W. Holt, R. Zhang, T. V. Esipova, S. A. Vinogradov, A. K. Glaser, D. J. Gladstone, and B. W. Pogue, "Cherenkov excited phosphorescence-based pO_2 estimation during multi-beam radiation therapy: phantom and simulation studies," Phys. Med. Biol. **59**(18), 5317–5328 (2014).
2. R. Zhang, A. Glaser, T. V. Esipova, S. C. Kanick, S. C. Davis, S. Vinogradov, D. Gladstone, and B. W. Pogue, "Čerenkov radiation emission and excited luminescence (CREL) sensitivity during external beam radiation therapy: Monte Carlo and tissue oxygenation phantom studies," Biomed. Opt. Express **3**(10), 2381–2394 (2012).
3. P. Vaupel, "Tumor microenvironmental physiology and its implications for radiation oncology," Semin. Radiat. Oncol. **14**(3), 198–206 (2004).
4. S. V. Apreleva, D. F. Wilson, and S. A. Vinogradov, "Tomographic imaging of oxygen by phosphorescence lifetime," Appl. Opt. **45**(33), 8547–8559 (2006).
5. R. Zhang, A. V. D'souza, J. R. Gunn, T. V. Esipova, S. A. Vinogradov, A. K. Glaser, L. A. Jarvis, D. J. Gladstone, and B. W. Pogue, "Cherenkov-excited luminescence scanned imaging," Opt. Lett. **40**(5), 827–830 (2015).

#331966 https://doi.org/10.1364/BOE.9.004217
Journal © 2018 Received 17 May 2018; revised 16 Jul 2018; accepted 6 Aug 2018; published 14 Aug 2018

Biomedical Optics EXPRESS

6. P. Brůža, H. Lin, S. A. Vinogradov, L. A. Jarvis, D. J. Gladstone, and B. W. Pogue, "Light sheet luminescence imaging with Cherenkov excitation in thick scattering media," Opt. Lett. **41**(13), 2986–2989 (2016).
7. P. Brůža, "MLC Planner," https://github.com/petrbruza/MLCplanner.
8. P. Vaupel, A. Mayer, and M. Höckel, "Impact of hemoglobin levels on tumor oxygenation: the higher, the better?" Strahlenther. Onkol. **182**(2), 63–71 (2006).
9. M. Nordsmark, J. Loncaster, C. Aquino-Parsons, S. C. Chou, M. Ladekarl, H. Havsteen, J. C. Lindegaard, S. E. Davidson, M. Varia, C. West, R. Hunter, J. Overgaard, and J. A. Raleigh, "Measurements of hypoxia using pimonidazole and polarographic oxygen-sensitive electrodes in human cervix carcinomas," Radiother. Oncol. **67**(1), 35–44 (2003).
10. J. L. Demers, S. C. Davis, R. Zhang, D. J. Gladstone, and B. W. Pogue, "Čerenkov excited fluorescence tomography using external beam radiation," Opt. Lett. **38**(8), 1364–1366 (2013).
11. T. V. Esipova, A. Karagodov, J. Miller, D. F. Wilson, T. M. Busch, and S. A. Vinogradov, "Two new "protected" oxyphors for biological oximetry: properties and application in tumor imaging," Anal. Chem. **83**(22), 8756–8765 (2011).
12. A. Y. Lebedev, A. V. Cheprakov, S. Sakadzić, D. A. Boas, D. F. Wilson, and S. A. Vinogradov, "Dendritic phosphorescent probes for oxygen imaging in biological systems," ACS Appl. Mater. Interfaces **1**(6), 1292–1304 (2009).
13. P. J. Shaw and J. R. David, "The point□spread function of a confocal microscope: its measurement and use in deconvolution of 3□D data," J. Microsc. **163**(2), 151–165 (1991).
14. P. Sarder and A. Nehorai, "Deconvolution methods for 3-D fluorescence microscopy images," IEEE Signal Process. Mag. **23**(3), 32–45 (2006).
15. D. J. Brady, A. Mrozack, K. MacCabe, and P. Llull, "Compressive tomography," Adv. Opt. Photonics **7**(4), 756–813 (2015).
16. D. J. Cuccia, F. Bevilacqua, A. J. Durkin, F. R. Ayers, and B. J. Tromberg, "Quantitation and mapping of tissue optical properties using modulated imaging," J. Biomed. Opt. **14**(2), 024012 (2009).
17. M. Sibai, I. Veilleux, J. T. Elliott, F. Leblond, and B. C. Wilson, "Quantitative spatial frequency fluorescence imaging in the sub-diffusive domain for image-guided glioma resection," Biomed. Opt. Express **6**(12), 4923–4933 (2015).
18. X. Chen, W. Lin, C. Wang, S. Chen, J. Sheng, B. Zeng, and M. Xu, "In vivo real-time imaging of cutaneous hemoglobin concentration, oxygen saturation, scattering properties, melanin content, and epidermal thickness with visible spatially modulated light," Biomed. Opt. Express **8**(12), 5468–5482 (2017).
19. A. P. Cuadros and G. R. Arce, "Coded aperture optimization in compressive X-ray tomography: a gradient descent approach," Opt. Express **25**(20), 23833–23849 (2017).
20. I. Odinaka, J. A. O'Sullivan, D. G. Politte, K. P. MacCabe, Y. Kaganovsky, J. A. Greenberg, M. Lakshmanan, K. Krishnamurthy, A. J. Kapadia, L. Carin, and D. J. Brady, "Joint system and algorithm design for computationally efficient fan beam coded aperture X-ray coherent scatter imaging," IEEE Trans. Comput. Imag. **3**(4), 506–521 (2017).
21. S. Tzoumas, D. Vernekohl, and X. Lei, "Coded-aperture compressed sensing X-ray luminescence Tomography," IEEE Trans. Biomed. Eng. **65**(8), 1892–1895 (2018).
22. C. M. Watts, D. Shrekenhamer, J. Montoya, G. Lipworth, J. Hunt, T. Sleasman, S. Krishna, D. R. Smith, and W. J. Padilla, "Terahertz compressive imaging with metamaterial spatial light modulators," Nat. Photonics **8**(8), 605–609 (2014).
23. S. W. Paddock and K. W. Eliceiri, "Laser scanning confocal microscopy: history, applications, and related optical sectioning techniques," in *Confocal Microscopy: Methods in Molecular Biology* (Methods and Protocols), S. W. Paddock, ed. (Humana, 2014).
24. M. Wojtkowski, T. Bajraszewski, P. Targowski, and A. Kowalczyk, "Real-time in vivo imaging by high-speed spectral optical coherence tomography," Opt. Lett. **28**(19), 1745–1747 (2003).
25. S. Yuan, Q. Li, J. Jiang, A. Cable, and Y. Chen, "Three-dimensional coregistered optical coherence tomography and line-scanning fluorescence laminar optical tomography," Opt. Lett. **34**(11), 1615–1617 (2009).
26. B. W. Pogue and M. S. Patterson, "Review of tissue simulating phantoms for optical spectroscopy, imaging and dosimetry," J. Biomed. Opt. **11**(4), 041102 (2006).
27. S. L. Jacques, "Optical properties of biological tissues: a review," Phys. Med. Biol. **58**(11), R37–R61 (2013).
28. M. Subbarao, T. C. Wei, and G. Surya, "Focused image recovery from two defocused images recorded with different camera settings," IEEE Trans. Image Process. **4**(12), 1613–1628 (1995).
29. F. Diaz, F. Goudail, B. Loiseaux, and J.-P. Huignard, "Increase in depth of field taking into account deconvolution by optimization of pupil mask," Opt. Lett. **34**(19), 2970–2972 (2009).
30. S. Webb, *Intensity-Modulated Radiation Therapy* (CRC Press, 2015).
31. G. Helmlinger, F. Yuan, M. Dellian, and R. K. Jain, "Interstitial pH and pO2 gradients in solid tumors in vivo: high-resolution measurements reveal a lack of correlation," Nat. Med. **3**(2), 177–182 (1997).
32. B. W. Pogue, J. Feng, E. P. LaRochelle, H. Bruža, H. Lin, R. Zhang, J. R. Shell, H. Dehghani, S. C. Davis, S. A. Vinogradov, D. J. Gladstone, and L. A. Jarvis, "Maps of in vivo oxygen pressure with submillimetre resolution and nanomolar sensitivity enabled by Cherenkov-excited luminescence scanned imaging," Nat. Biomed. Eng. **2**(4), 254–264 (2018).

Biomedical Optics EXPRESS

33. R. Zhang, S. C. Davis, J. L. Demers, A. K. Glaser, D. J. Gladstone, T. V. Esipova, S. A. Vinogradov, and B. W. Pogue, "Oxygen tomography by Čerenkov-excited phosphorescence during external beam irradiation," J. Biomed. Opt. **18**(5), 050503 (2013).

1. Introduction

Radiation therapy induces Cherenkov light emission within tissue, and this signal provides potential for direct molecular sampling of the tissue microenvironment [1–4]. The approach to using Cherenkov Excited Luminescence Scanned Imaging (CELSI) was examined here, specifically varying the spatial patterns used to excite Cherenkov light from megavoltage (MV) X-rays in external beam radiation therapy (EBRT) [5,6]. CELSI can provide three-dimensional luminescence images through layer-scanned Cherenkov light sheet, which is carried out by movements of the multi leaf collimator (MLC) on the linear accelerator (LINAC), which is commonly used to provide conformal shaping of radiotherapy treatment beams [7]. This application has been experimentally demonstrated *in-vivo* and is hopeful for clinical trial use, taking advantage of the dynamics already inherent in radiotherapy treatments [5,6]. In this study, progressive approaches to scan beam size and shape were explored to understand how incorporation with dynamic treatment plans might occur.

Since tissue partial pressure of oxygen (pO_2) is well known to affect the efficacy of radiotherapy [1,8,9], imaging this signal has been a primary focus of previous CELSI studies. In order to image pO_2 in tissue for EBRT, megavoltage (MV) photon beams have been utilized to induce Cherenkov emission in thin sheets within the tissue which in turn excites an oxygen-sensitive phosphorescent probe. An example is excitation of Platinum (II)-G4 (PtG4) [10–12] via Cherenkov light emission, which efficiently absorbs blue light (λ_{max} = 435nm) and emits phosphorescence in the NIR region (λ_{max} = 772nm). Epi-illumination based CELSI in tissue allows for imaging to a depth of one centimeter or more, depending on the fluorophore concentration and radiation dose used. The scattering-induced blurring can be compensated by deconvolution processing based on the point spread function (PSF), evaluated by radiative transport models [6,13,14]. The hypothesis examined in this study was that when designing this irradiation scheme, the beam shape could be chosen to optimize the spatial-resolution of recovered CELSI images. Further, it might be possible that existing clinical treatment plans allow for high resolution imaging.

Patterned illumination schemes have been investigated more recently with the emergence of compressed sensing, where computed image recovery is utilized to improve the image quality without extra radiation exposure and/or acquisition time [15]. While the ultimate extent of compressed sensing methods uses complex patterns, the methodology for this could include a simpler spatial-frequency-domain imaging (SFDI) approach or more complex techniques such as used in coded aperture imaging (CAI). Current SFDI instruments typically use projected spatially modulated light, projected onto the sample, and then knowledge of the illumination patterns are used to demodulate the images [16–18]. CAI requires a coded mask placed either, in front of the radiation beam source to shape the incident beam, and at the detector to block the transmitted beam and disambiguate scatter angles [19–21]. For both of these structured imaging modalities, the excitation beam is modulated by a projector or a coded aperture, and the measured reflectance or transmittance is demodulated in post-processing. This modulation-demodulation method (MDM) has the capacity to mathematically filter the low frequency out-of-focus scattered photons beyond the depth of field of the imaging objective. For the MDM process using a point raster scanned beam, the narrow beam acts as a virtual pinhole, analogous to the emission light captured through a pinhole in confocal microscopy. Diversification of the illumination pattern based on an MLC is clinically convenient in CELSI and could be time-saving, and in principle the type of spatially modulated patterns could be extremely beneficial to provide high resolution imaging. In particular, using coded apertures in conjunction with multiplexed illumination can reduce the acquisition time, given that projections from more than one source may be acquired in a single step [19].

Biomedical Optics EXPRESS

Motivated by the idea of using patterned illumination schemes, the study here examined if the spatial resolution and contrast recovery of CELSI could be improved on using different spatial illumination patterns and post processing with MDM. The input radiation beam was modulated and raster-scanned by programming the MLC, and post-processing demodulation was performed by deconvolving the measured luminescence image with the kernel function of the Cherenkov image. This approach, referred to as MDM-CELSI, examined several EBRT-compatible MLC plans, and specifically how the measurement geometry affected the acquisition time, and radiation does. Modulation of the radiation (X-ray) beam was investigated using basic illumination patterns including squares and lines, and multiple combinations of these.

2. Methodology

2.1 Incidence modulation

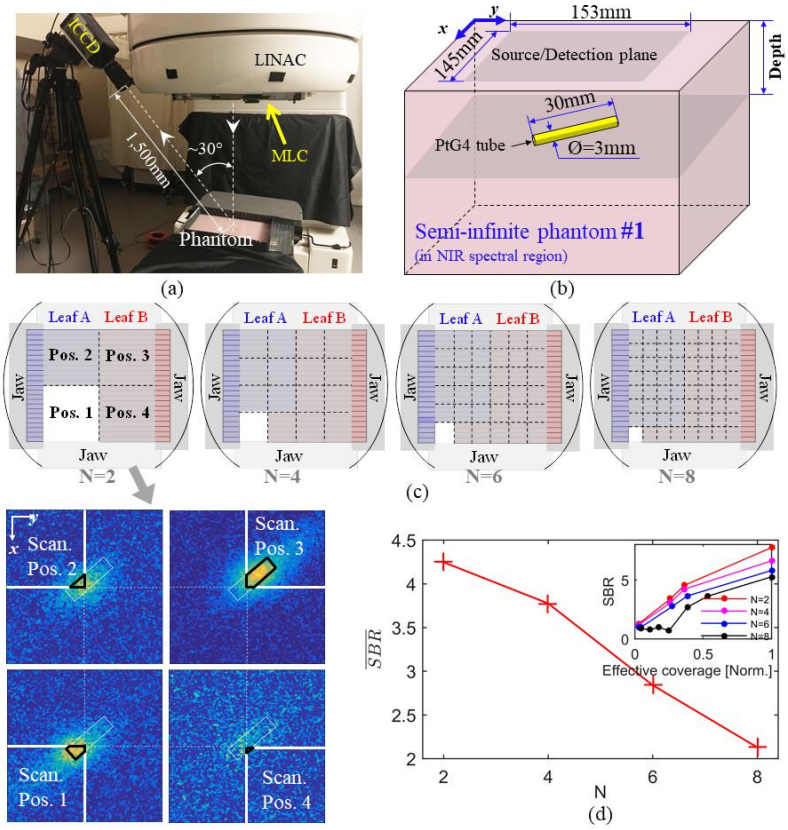

Fig. 1. The experimental setup used to investigate the effect of radiation beam size is shown in (a) with a photo of the experimental setup with LINAC, phantom and ICCD camera; (b) the internal phantom geometry; (c) the basic N × N square-raster scanning patterns tested initially with different pixel areas and the luminescence images measured for N = 2 (below this), and (d) the calculated Signal to Background ratio (SBR) versus target area for N = 2, 4, 6, and 8, respectively.

A clinical radiotherapy accelerator (Varian Clinac 2100 CD, Varian Medical Systems, USA) was used to generate a pulsed beam with the following parameters: photon beam energy of 6 MV, dose rate of 600 monitor units per minute (MU/min), at a fixed repetition rate of 360 Hz, and a ~3.25 μs pulse duration. The X-ray beam impinged on the tissue-equivalent phantom, embedded with a 70 µM PtG4 target (inner diameter Ø ≈3mm, and length of 30mm) at a depth of ~1.2cm, which is detailed in Fig. 1(a) and (b). The camera with a focal length of

Biomedical Optics EXPRESS

85mm and f/1.2 lens was mounted close to LINAC as shown in Fig. 1(a), resulting into an inclined angle of ~30° and a distance of ~1,500 mm from the sample. The luminescence signal was detected with time-gated acquisition of the ICCD (100 μs integration time and 4.26 μs delay after each x-ray pulse). The luminescence images were acquired with 100 × gain on the ICCD intensifier, 30 pulses integrated on-chip as accumulations prior to each frame readout, and 2 × 2 hardware pixel binning at readout, from chip size of 1024 pixels × 1024 pixels. Cherenkov images were acquired in the same way, but with 0 μs pulse delay and a 3.5 μs integration time. Measurement at an increased pulse delay of ~500 μs was also acquired as 'background images' from the same field of view (FOV), which was used to subtract out stray signals in the camera and room.

In order to utilize LINAC-based EBRT for the CELSI illumination plan, a patterned beam design must be created with consideration of the geometry and orientation the MLC, which does put some limit onto what is possible. For the MLCs used here, the lateral length (along the direction orthogonal to movement) of a single MLC leaf was 5mm with step sizes of 0.1mm; the smallest point excitation available realistically was on that spatial scale. The geometry of these MLCs are optimal for targeting single-connected regions or distributions along the central axis, but it can be impossible to form more complicated shapes that might be optimal, like the Hadamard matrices for example [22]. X-ray beams were raster-scanned with different sized squares as shown in Fig. 1(c), which was performed by delivering a custom dynamic dose plan, created in MLC code [13]. The measured luminescence images for an N × N (N = 2) raster-scanned illumination are shown below Fig. 1(c), where the regions encircled with black lines are the pixel areas included within the radiation beam, named as the effective coverage. The relationship of Signal to Background ratio (SBR) with the effective coverage, and N, are shown in Fig. 1(d), where the SBR can be found strongly dependent upon both. A reasonable square/beam area could be more than 1mm^2.

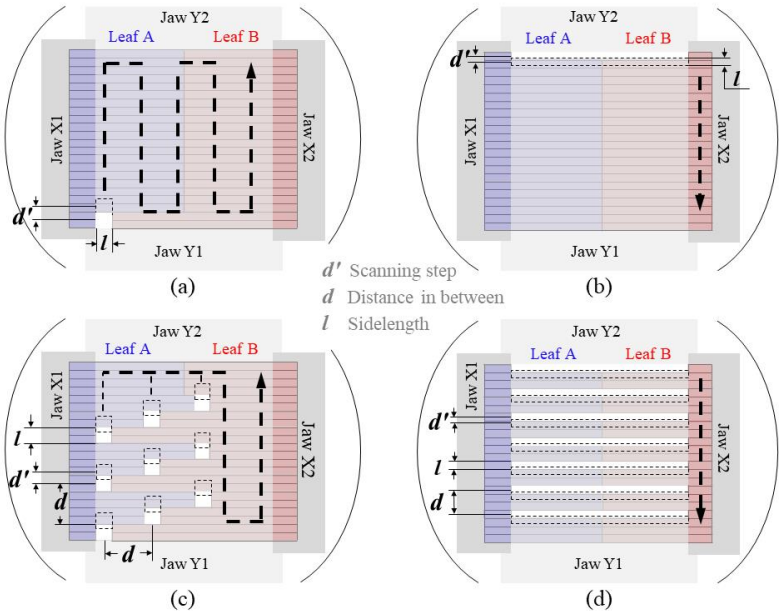

Fig. 2. Two basic illumination patterns studied are displayed from the top-view of the MLC, including: (a) a single square, raster scanned in 2 dimensions across the entire field of view, (b) a thin line, scanned in one dimension vertically down through the field, (c) a multiple-square pattern which is scanned; and (d) a multiple-line pattern scanned downwards. The blue and red rectangles represent leaves of Groups A and B, respectively, while the black dashed frames indicate movement to the next scanning positions, and the thicker dotted arrow lines indicate the total movement plan.

Biomedical Optics EXPRESS

To accelerate the acquisition process, several square-illuminations are simultaneously enabled, which allowed for reduction of total scan time. As a proof-of-concept, one type of multi-square illumination with equal spaces is shown in Fig. 2 (c), where the dashed squares represent the next scanning positions. The multi-square distribution depends on following two parameters: (1) the square side-length l, which is found by a compromise between spatial resolution and measurement SNR; and (2) the beam pitch $P = d'/l$, where d' is the step size. P <1.0 denotes there is an overlap in between the continuous squares and vice versa. For full-field illumination, we assume P = 1, which indicates a contiguous scanning for adjacent positions. For multiple scanning, $d' = (\mathrm{N}l - d)/(\mathrm{N}-1)$, where d is distance in between each square, and the total scan positions should be N^2 times the number of squares in a multi-square shape. To be comparable with the point-raster strategy, d should be large enough to avoid cross-talk effect. The minimum of d ($d_{\min}$) depends on the system SNR, which is the critical source-detector separation estimated by fluorescence Monte-Carlo simulation. For typical optical properties of normal human tissue under the wavelength λ = 772nm (PtG4 phosphorescence peak), *i.e.*, the absorption coefficient μ_a, scattering coefficient μ_s, and anisotropic factor g values common in soft tissue, at $\mu_a = 0.01\mathrm{mm}^{-1}$, $\mu_s = 10\mathrm{mm}^{-1}$, and $g = 0.9$, $d_{\min}$ is near 2mm.

As an alternative way to accelerate acquisition, line-scan field illumination has been demonstrated in confocal microscopy [23], optical coherence tomography (microscopy) [24,25], and laminar optical tomography [25]. Further accelerations can be similarly reached by multiple enablement strategy, named as multi-lines illumination, as shown in Fig. 2(d). Also, the distance in between each line should be greater than d_{SNR}. Comparisons between point- and line- shaped patterns with different combinations of l and P was examined.

2.2 Image demodulation

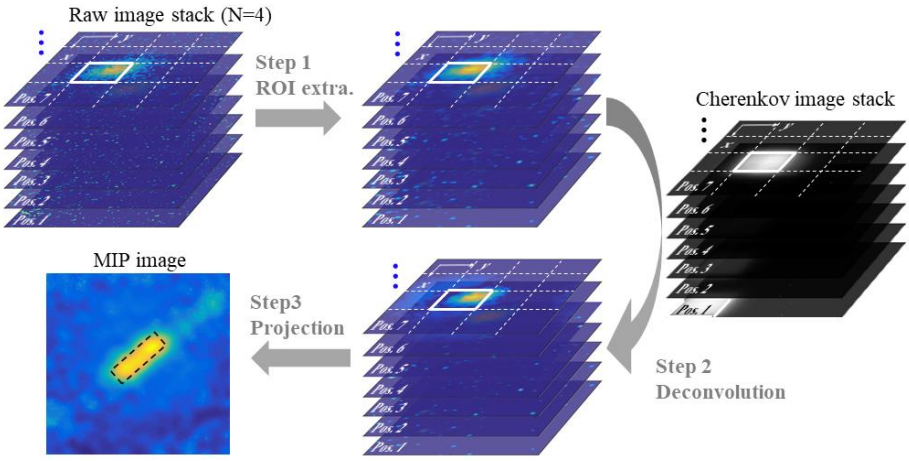

Fig. 3. Diagram of the patterned-CELSI (N = 4) postprocessing sequence involving acquision of both luminescence and Cherenkov at each of the raster scanned positions and region of interest (ROI) extraction (step 1) followed by deconvolution of the luminescence by the Cherenkov shape (step 2) and combining together for a MIP image (step 3). The dashed black square in the MIP images indicates the true position of the target.

The procedure of image demodulation is illustrated by the flow chart in Fig. 3. For simplicity, a 2D square-raster scan is illustrated here with 4 × 4 uniformly distributed scanning positions. The resulting input raw image is composed of 16 pixels corresponding to the 16 positions. The steps are: (1) the raw images were processed frame-by-frame to mainly extract the region of interest through subtracting 'background' ones; (2) the Cherenkov image was used as the

Biomedical Optics EXPRESS

kernel function to deconvolve the corresponding luminescence images; and (3) demodulation is done by combing all the frames into a Maximum Intensity Projection (MIP) image. Considering the multiple deconvolutions in step 2, an economical one-step deconvolution algorithm was used for *i*th scanning position, which can be formulated as

$$\mathbf{X}_i = \begin{cases} F^{-1}\left\langle \dfrac{F\langle \mathbf{Y}_i \rangle(w)}{F\langle \mathbf{C}_i \rangle(w)+\varepsilon} \right\rangle, if\ |w| < R \\ 0, if\ |w| < R \end{cases}, \quad (1)$$

where **Y** and **X** is the raw and undistorted luminescence image, respectively; **C** is the Cherenkov image; ε is an infinitesimal integer; and $F\langle\cdot\rangle$ and $F^{-1}\langle\cdot\rangle$ represent Fourier and inverse Fourier transforms, respectively. Note that the range of spatial frequencies w can be physically limited in a radius of R ($\in [1.5\,2.5]$ in this paper), which is regulated by a specified beam pattern, and can be estimated instead through the high signal-to-background ratio Cherenkov image.

3. Result

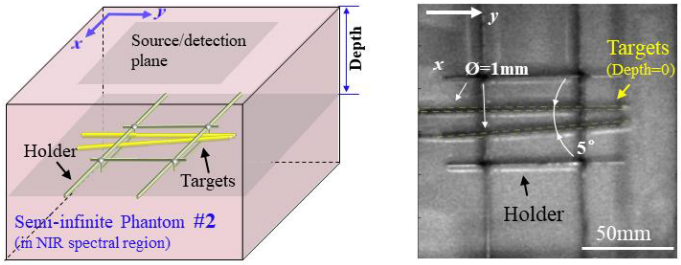

Fig. 4. Phantom experiments for image fidelity demonstration, with (a) an 3D schematic of the Intralipid-blood tissue phantom with two capillaries inside filled with PtG4 (yellow cylinder); and (b) a photograph of this geometry with target depth being zero, for illustration.

A series of phantom studies were carried out using a tissue-equivalent phantom, which consisted of 1% Intralipid and 1% porcine blood per unit volume of solids, with absorption and reduced scattering coefficients estimated to be $\mu_a = 0.01\text{mm}^{-1}$ and $\mu_s' = 1\text{mm}^{-1}$ in the NIR spectral region at 800nm [26,27]. The measurement geometry is shown in Fig. 1, and the phantom adopted (#2) is illustrated in Fig. 4, where two plastic capillaries (inner diameter Ø≈1mm) containing 70 μM PtG4 solution were placed with an angle of 5° in between as shown in Fig. 4. The angled capillaries were designed to pick up a reasonable Y-period between unresolvable and completely resolved status for X-profile analysis. A holder, which is fixed to the wall of phantom container, was used to clamp the capillaries. Without specific notification, the depth of target is 8mm.

3.1 Comparisons between line- and square scanning pattern

In the first study, line- and square- raster scanning were compared for P = 0.50, 0.33, and 0.25, respectively, and a fixed square size of l = 77 mm, as shown in Fig. 5. To quantify the spatial resolution performance, a metric of success was introduced, defined as $R = (\mathrm{I}_{\max} - \mathrm{I}_{x=69\text{mm}})/(\mathrm{I}_{\max} - \mathrm{I}_{\min})$, with $\mathrm{I}_{\max}$ and $\mathrm{I}_{\min}$ being the maximum and the minimum in the x-profile of the image, essentially providing a relative measure of contrast recovery. Considering the possible artifacts & distortion for the plastic capillaries walls themselves and uneven PtG4 distribution inside, X-profiles for the period included by the two white dashed lines were averaged to obtain a more robust estimate of R. Since there was a 5° angle in

Biomedical Optics EXPRESS

between the two rods, X-profile was not accurately specified for a fixed Y-value in this case. With this definition, R = 1 represents that the two targets can be completely separated, with full contrast recovery. In the characteristics of the human vision system, it is normally assumed that two targets are distinguishable for R>0.1 (when a 10% dip in intensity is observed between them). In addition to spatial resolution, radiation dose and acquisition time were also estimated and all are listed in Table 1. Acquisition time was calculated as: "Dose(MU)" /"Dose rate(MU/min)", which just estimated total scanning time, excluding mechanical switching issues which vary from machine to machine. We assume that Cherenkov emission, luminescence and background signals can be read out in one pulse cycle, which is the time period between two LINAC pulses. This can be realized with a time-resolved camera by specifying the corresponding pulse delays.

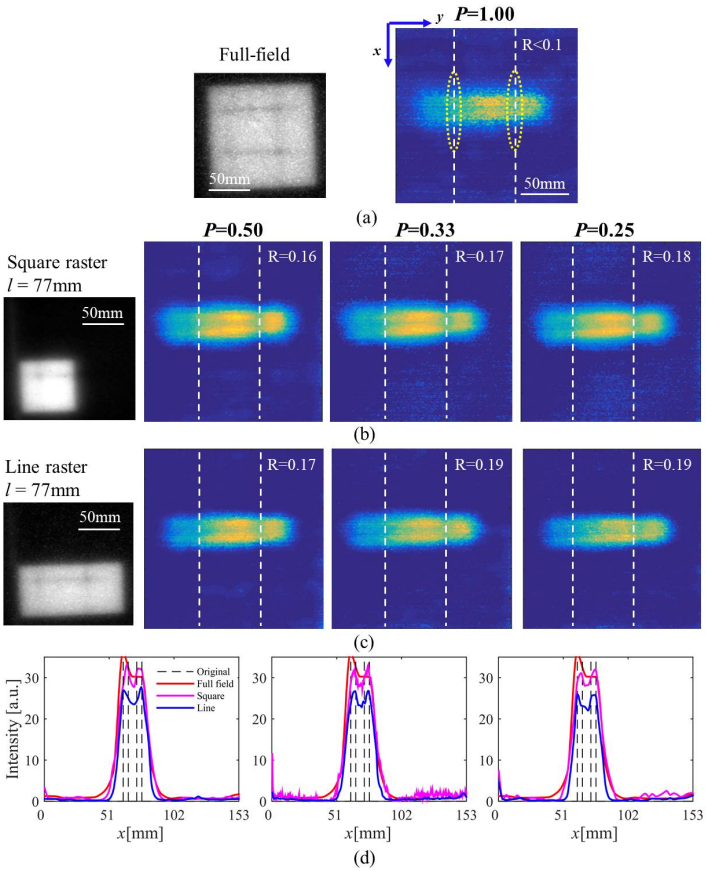

Fig. 5. Luminescence (color) and Cherenkov (greyscale left) images are shown, as measured under (a) full-field covering the entire frame, (b) a larger square 2D-raster scanned field, and (c) a thick line 1D-raster scanned. The corresponding X-profiles below (d) were averaged along the Y-axis direction for a distance in between the two white dashed lines indicated in (a)-(c). The value of R is inset in each image to qualify contrast recovery.

Table 1. Comparisons between line and point raster for P = 0.50, 0.33, and 0.25, respectively, and a fixed l = 77mm.

	Dose (MU)			Time (s)			R		
P	0.50	0.33	0.25	0.50	0.33	0.25	0.50	0.33	0.25
Full field	138			14			<0.1		
Point raster	311	466	615	124	221	345	0.16	0.17	0.18
Line raster	184	276	345	42	55	69	0.17	0.19	0.19

Biomedical Optics EXPRESS

In general, beam projections shaped by the MLCs are clinically defined by the targeting for the tumor region. The most unresolved shape used is a squared 'full-field' shape, with its Cherenkov image shown in Fig. 5(a). It is worth noting that, the full-field region was slightly smaller than FOV to conserve the diffused edges for both Cherenkov and luminescence images, to allow for complete measurements of the kernel function by the raw Cherenkov image for the deconvolution. For the luminescence imaging, one artifact noted was that the metal-made holder could attenuate some fluorescence emission, which led to 'slightly-dimmer regions' on the PtG4 target as indicated with yellow dashed circles, but these was avoided in the analysis, and not present in the line scans analyzed, Fig. 5(d).

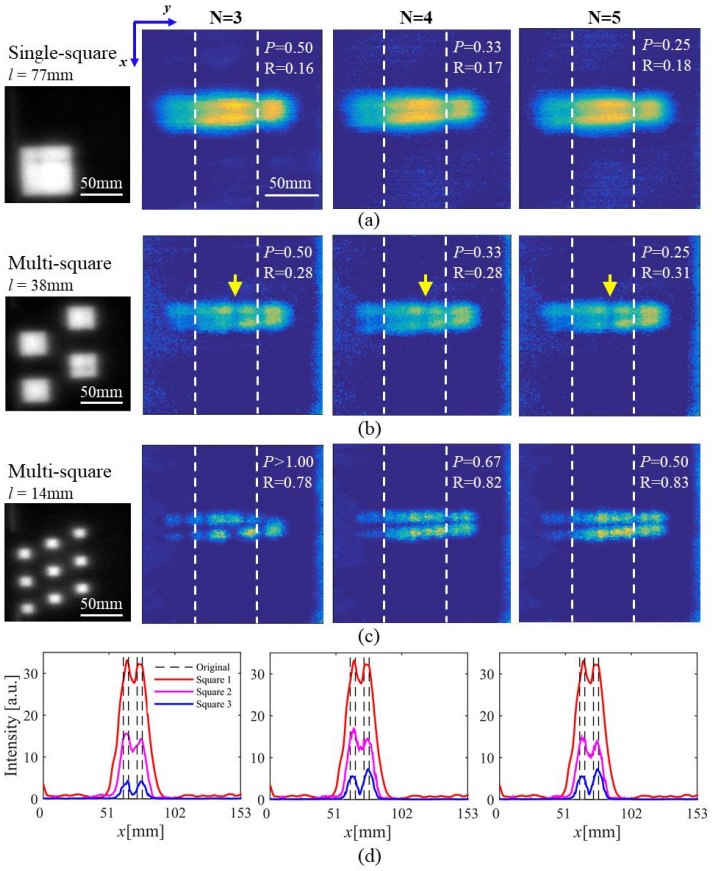

Fig. 6. Luminescence (color) and Cherenkov (greyscale left) images as measured under (a) large 77mm block beam raster scanned, (b) a series of 4 parallel 38mm square raster scanned beams, and (c) a series of 9 parallel 14mm square raster scanned beams. The corresponding X-profiles (d) were averaged along the Y-axis in between the two white dashed lines indicated in (a)-(c). N values decide the scanning step *d'*. *R* values recovered are overlaid on each luminescence image, showing the large improvement in *R* with smaller beam sizes. (A full scanning video of merged Cherenkov and deconvolved Luminescence image sequence for N = 4 is available in Visualization 1).

Several conclusions can be drawn from Fig. 5. (1) Both square- and line- raster results show higher contrast recovery (R>0.15) than that of the full-field ones (R<0.1). Basically, the two capillary rods cannot be discriminated in the 'full-field' image. (2) Image resolution seldom varies with scanning step since no space exists in between two adjacent squares, *i.e.*, P<1. However, the recovered image would degrade a lot if P>1, *e.g.*, the capillary rods were found to be discontinuous in Fig. 6(c) when P>1. (3) In this case, the line-scan results slightly outperformed the square point-scan ones. This could be explained by the nearly parallel

Biomedical Optics EXPRESS

direction between the capillaries placed and the illumination orientation. In other words, resolution would be reduced if the two directions were orthogonal. For example, as pointed out by the yellow arrows in Fig. 6(c), some dimmed regions could be more clearly discerned in square point-scan images, which, however, are not visible in line-scan results as shown in Fig. 6(b). These regions were highly resolved in Fig. 7, and also visible in Fig. 8. An improvement to the line-scan methods would be multi-direction scanning, which could render a full-direction resolution enhancement, however, this would come at the cost of doubling the radiation dose and acquisition time.

Multi-point scanning of squares is therefore demonstrated above to be ideal compromise between optimal resolution, minimal scan time and minimal dose. Further investigations were aimed at optimization of the pattern parameters as discussed in Section 2.A, *i.e.*, l and P. Three kinds of square patterns were deliberately designed for this test, with their Cherenkov images displayed in greyscale as shown in Fig. 6, progressing from larger to smaller block sizes with separation of them sufficiently large to avoid any crosstalk. From the luminescence images in Fig. 5, R-value was not strongly dependent upon the value of d'. In comparison, the square size characterized by side-length l imposed a significant influence on spatial resolution, *e.g.*, from the images (bottom line of Fig. 5) with $R<0.2$ when l = 77mm to those (middle line of Fig. 5) with $R>0.77$ when l = 14mm. However, the measurement intensity of the former cases was 5 times higher than the latter ones, which is in agreement with the conclusions of intensity versus illumination area in Section 2.1. Consequently, we applied a trade-off, where a side length of 38.3mm and P = 0.33 were tested here.

Biomedical Optics EXPRESS

3.2 Imaging for varying target depths

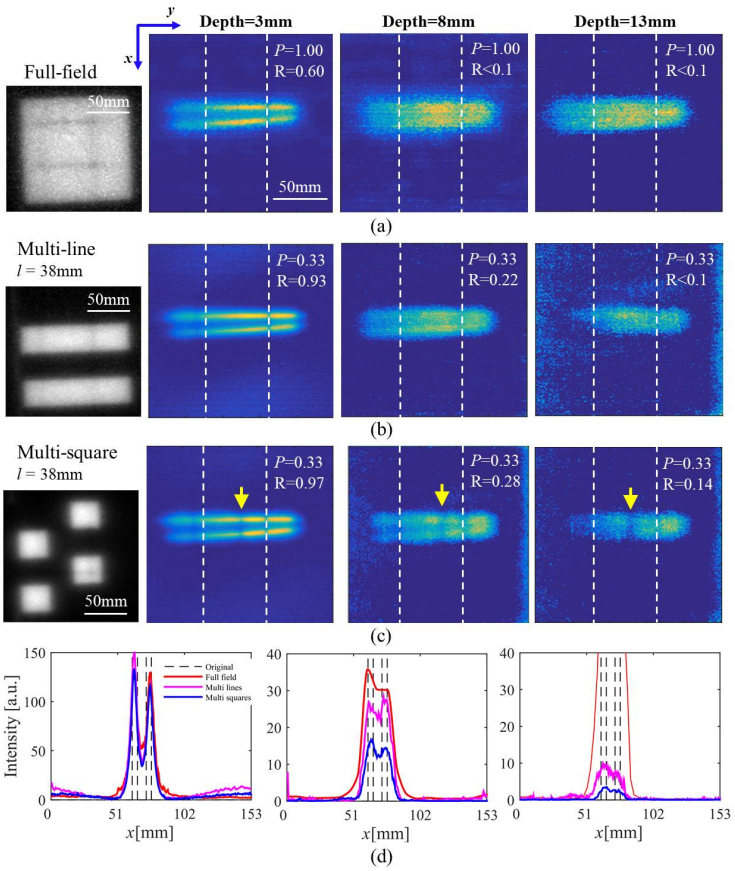

Fig. 7. Luminescence (color) and Cherenkov (greyscale left) images as measured under (a) full-field, (b) square raster scanned, and (c) line raster scanned beams, for target depths of 3, 8, and 13mm, respectively, from left to right columns. The corresponding X-profiles (e) were averaged along the X-axis in between the two white dashed lines indicated in (a)-(c). The *R* values of each scan are overlaid on each luminescence image, showing the large decrease with depth into the medium, but that the raster scanned square beams (c) allow sufficient *R* resolution down to the lowest depth of 13mm.

In this section, the effect of increasing target depth was analyzed. It can be seen from Fig. 7 that, all the methods could provide clearly discerned images for the smallest target depth. In comparison, the full-field image presents a result of lower spatial resolution as well as SNR, and an available imaging depth of less than 8mm. For the deepest target at 13mm, only the imaging result with the square beams could provide a spatial resolution of R>0.1. Since the deblurring strategy herein only considered Cherenkov photon scattering, the recovered images for large-depth targets embedded in a scattering medium should have diffused edges. Depth-corrections for fluorescence photon scattering have been widely developed in (fluorescence) diffuse optical tomography. Besides, depth-related image deconvolution has been customized for CELSI in previous work [6].

Biomedical Optics EXPRESS

3.3 Modulation transfer function analysis

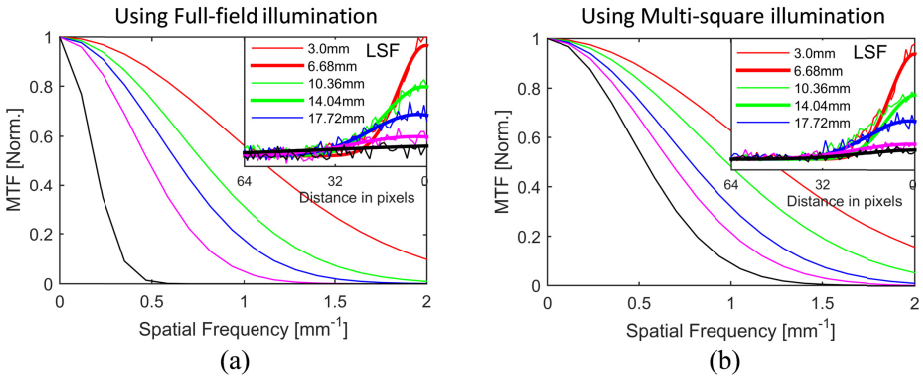

Fig. 8. Normalized Modulation Transfer Function curves estimated for (a) full-field, and (b) multi-square illuminations. The insert curves are corresponding line spread functions and their Gaussian fitting results.

To quantify spatial frequencies that can be resolved versus depth, a phantom embedded with a single target (capillary of Ø≈1mm, filled with 70 μM PtG4) was imaged to obtain the Modulation Transfer Function (MTF) from line scan data. Results as measured under both full-field and multi-square illumination are plotted in Figs. 8 (a) and (b), respectively, where the squared beam shape was scanned with an optimized parameter set at l = 38mm and P = 0.25. The line spread functions (LSF) are inset correspondingly and fitted to Gaussian curves in the subplots, and demonstrate the available spatial frequencies from which information can be obtained.

Table 2. Inverse of limiting spatial frequency (50% of the MTF amplitude) defined at varying depths for full-field and multi-square illumination.

Target depth	3.0mm	6.7mm	10mm	14mm	18mm
Full field	0.9mm	1.3mm	1.6mm	2.1mm	5.2mm
Multi square	0.8mm	1.0mm	1.2mm	1.5mm	1.8mm

Spatial resolutions achievable are related to the inverse of the MTF function where there is measurable amplitude, and here it was taken as 50% of the maximum. These are defined at different target depths, as recorded in Table 2, where the effective lower limit on resolution was estimated. It can be seen from Table 2 that, the difference in spatial resolution between these two methods increases significantly from roughly 0.1mm at a target depth of 3mm to a difference of 3.4mm at 18mm. For a target depth of 14mm, both full-field illumination and the scanned multi-square method retain reasonable resolution near 1mm, but just slightly beyond this depth (18mm depth) the true capillary diameter could not be resolved with full field illumination but likely could be with the scanned multi-square approach.

3.4 Correction for defocused blurring

To acquire high signal intensity or measurement SNR, a large-NA lens is generally applied for fluorescence imaging, which however renders a limited depth of field (DOF). The adopted lens used in this study was FL = 85mm and f/1.2, for instance, which provides only a DOF = 9.4cm for coupling to the PI-MAX4 camera. Since defocus blur can be seen simply as the convolution between a sharp image and a blur kernel, one can solve for the sharp image again by deconvolving the blurred image with the same point spread function (PSF) used to blur the original sharp image [6,28]. However, the PSF has to be either estimated by scaling a depth-dependent PSF, or experimentally obtained through capturing the out-of-focused target with different camera-target distance [29].

Biomedical Optics EXPRESS

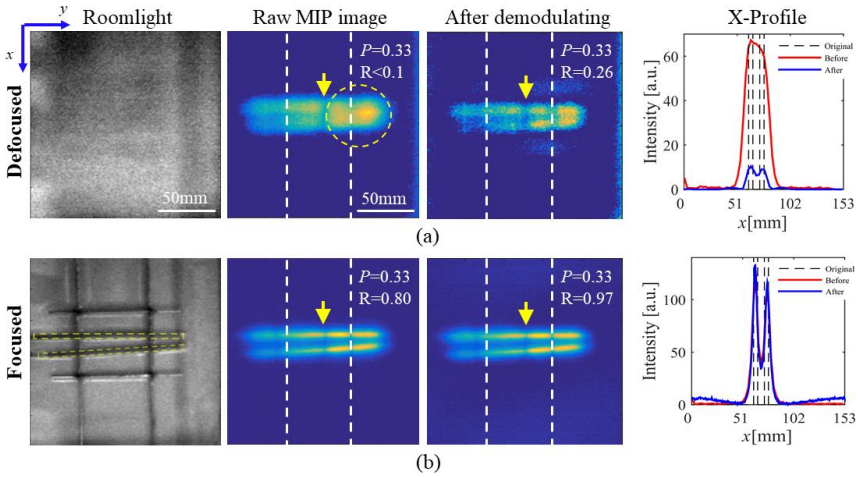

Fig. 9. (a) Defocused and (b) focused imaging results are shown. From left to right the columns are photograph, then luminescence images before and after demodulation, and the corresponding X-profiles, respectively. The X-profiles are averaged for Y-distance in between the two white dashed lines indicated.

A small target depth of 3mm was investigated to highlight the value of this deblurring by inducing a defocusing acquisition instead of photon scattering. The experimental results are shown in the Fig. 9(a), where luminescence images before and after demodulating and correction are displayed correspondingly. As references, all-in-focus images are shown in the lower line of Fig. 9. It can be seen from the defocused image before correction, the two capillaries are hard to separate (R<0.1) and even overlapped with each other at the place indicated by the yellow dashed circle. After correction, the capillaries can be discerned with R increasing to 0.26.

4. Clinical geometry studies in breast scanning

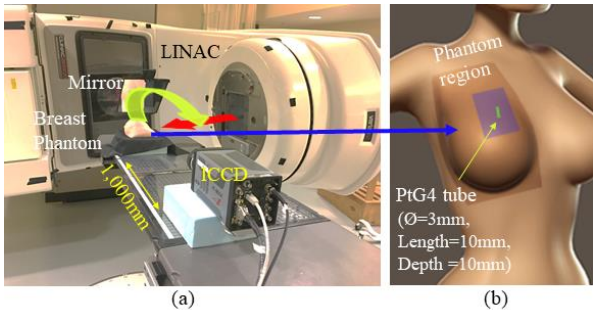

Fig. 10. CELSI applied in breast EBRT: (a) measurement geometry, and (b) schematic of a full-size right-sided breast phantom. A tube filled with 70 μM PtG4 was embedded at a depth of 10mm to simulate a lymph node. The red and green arrows track X-ray and luminescence signals, respectively. The blue rectangle region in (b) is the field of view.

Most EBRT treatment plans in patients dynamically shape the beam with the MLCs and Jaws within the LINAC, targeting the tumor region and minimizing dose to nearby critical structures. As a result, it was hypothesized that the natural spatial modulation done in clinical radiotherapy could be used to achieve an enhanced CELSI, based upon how the beams were formed. To investigate this, we used three typical breast treatment plans, *e.g.*, a conformal radiation therapy (3D-CRT), an over modulated 3D-CRT (3D-CRT^{OM}), and an Intensity Modulated Radiation Therapy (IMRT) [30]. In addition, a dynamic wedge (DW) plan was investigated, which instead uses the Jaws slowly closing to the desirable shape. A full-size

Biomedical Optics EXPRESS

breast phantom with tissue equivalent optical properties was created, CT-scanned and the shape transferred to the Eclipse treatment planning system (Varian Medical Systems, Palo Alto, CA) for radiotherapy treatment planning. In these treatment plans, gantry angle of 270° or 280° was used for medial tangent beam, and angles of 90° or 100° was used for lateral tangent for right breast cases. Radiation does used for 3D-CRT, 3D-CRT^{OM}, DW and IMRT were 194MU, 246MU, 204MU, and 210MU, respectively, with fixed beam energy of 6MV (note, 100MU corresponds to a dose of 1 Gy at the isocenter of the beam at D_{max} depth). The measurement geometry is shown in Fig. 10(a), where a mirror was used to reflect the outgoing luminescence light into a horizontally positioned camera. The breast phantom was positioned in a whole-body model in Fig. 10(b). The camera worked at a frame-rate of 10fps to make a tradeoff between measurement SNR and time resolvable snapshot.

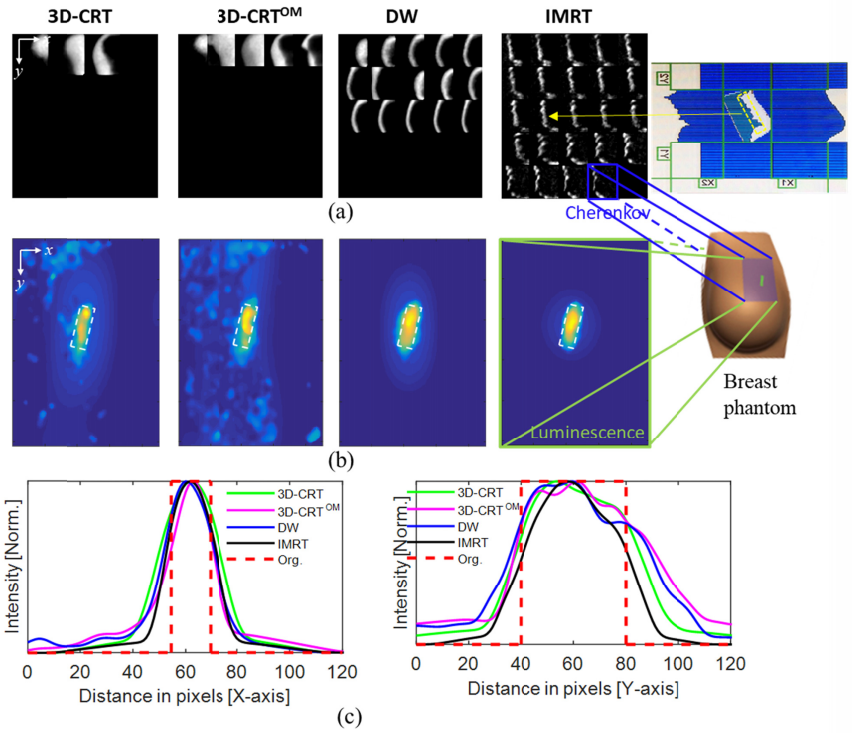

Fig. 11. CELSI results with beam scanning with clinical breast treatment plans. (a) Difference Cherenkov images merged with deconvolved luminescence ones showing the beam shape differences; (b) luminescence images reconstructed of the 10mm deep target; and (c) corresponding profiles along the two orthogonal axes through the target centroid point. (A scanning video of merged Cherenkov and deconvolved Luminescence image sequence is available in Visualization 2 for both the original and difference results).

Investigations on these beam shapes show that most of them were confirmed with widely opening MLCs or Jaws. As discussed before, proper beam size is crucial to obtain a high fidelity images. To maximize the spatial value of the kernel in the modulation-demodulation method, a finite differencing process was used in between original frames to get difference images and the resultant luminescence images were then differenced correspondingly, as illustrated in Fig. 11(a). Note that irradiation in the DW plan was performed in an edge scanning way, which then was converted to a linescan one after the difference operation. Edge scanning was also tested with the IMRT plan, while the difference is that the IMRT instead used the MLCs to shape the beam. Since it was hard to make all the leaves move at a same speed, an original line-shaped beam was distorted as shown in Fig. 11(a). However, because of this distortion, the resultant beam was actually shaped somewhat between a full

Biomedical Optics EXPRESS

linescan or square beam scan. A screen shot from the MLC console recorded the transient status of all the leaves corresponding to one scanning position, as shown in Fig. 11(a).

The recovered images with the proposed method are shown in Fig. 11(b), with their X- and Y- profiles plotted in the left and right positions of Fig. 11(c), respectively. Significant background noise was found in the first two results, the 3D-CRT and 3D-CRT^{OM} plans respectively, because the beamlets were less effective at excitation as shown in Fig. 11(a), leading to a reduced frame rate in the image sequence acquired. For the latter two plans, the IMRT result performed better, which was due to the combined beam shapes between a line and a square, leading to an additional improvement along Y-axis as shown in Fig. 11(c). At present, the IMRT plans are used to treat the more complex cancers, *e.g.*, head and neck, and central nervous system [30]. For the images recovered with 3D-CRT and 3D-CRT^{OM} plans, due to the insufficient effective inputs, targets are erroneously positioned and a bit oddly formed because of the limited beam shapes.

5. In-vivo mouse studies

In this section, the MDM-CELSI technique was used for 3D imaging of a tumor in a living mouse, and the pO_2 concentration was estimated for both tumor and non-tumor regions. All animal procedures were approved by the Dartmouth Institutional Animal Care and Use Committee, and the studies here were carried out in compliance with these approved procedures. Nude female mice were purchased at 6 weeks of age from Charles River Labs. After a week of acclimatization, animals were used for injections of 10^5 MDA-MB-231 cells under the skin on one upper limb flank of the mouse in individual 0.050 ml injections. After approximately 3 weeks of growth, when a tumor with an average of 6 mm diameter was observed on the flank, the animals were then used for imaging studies. All mice were under general anesthesia of inhaled isoflurane at 1.5% in flowing air through a nose cone throughout imaging. A total of 50ml of 25μM PtG4 was directly injected into the tumor and normal regions on both blanks. For LINAC settings, a 6MV beam with a dose rate of 600MU/min was used. Dynamic MLC plans were used to generate the specified beam shapes for 3D CELSI acquisition and subsequent pO_2 estimation, respectively. In order to recover the pO2, a range of delays were created between the linac pulse and the emission collection, so that the emission intensity lifetime at each position could be recovered. Finally, this animal was imaged in the IVIS Spectrum CT system for X-ray tomography for spatial reference.

5.1 3D rendering

To render a 3D view, the beam was introduced in the lateral direction as a sheet, which was scanned bottom to top, typical of previous CELSI results, and then images captured by a vertically placed camera could be 3D stacked along depth direction [6]. A room light image under the same FOV was captured and is displayed in Fig. 12 (a). The resultant Cherenkov combined with demodulated luminescence images at each scanning positions are shown in Fig. 12(b). Similar to the scanning process in Section 4, Cherenkov beamlets swept over the target areas, which gives access to the MDM method. As a comparison, we show the raw and processed MIP images in Fig. 12(d), where the corresponding X- and Y- profiles across the tumor region is also present.

Biomedical Optics EXPRESS

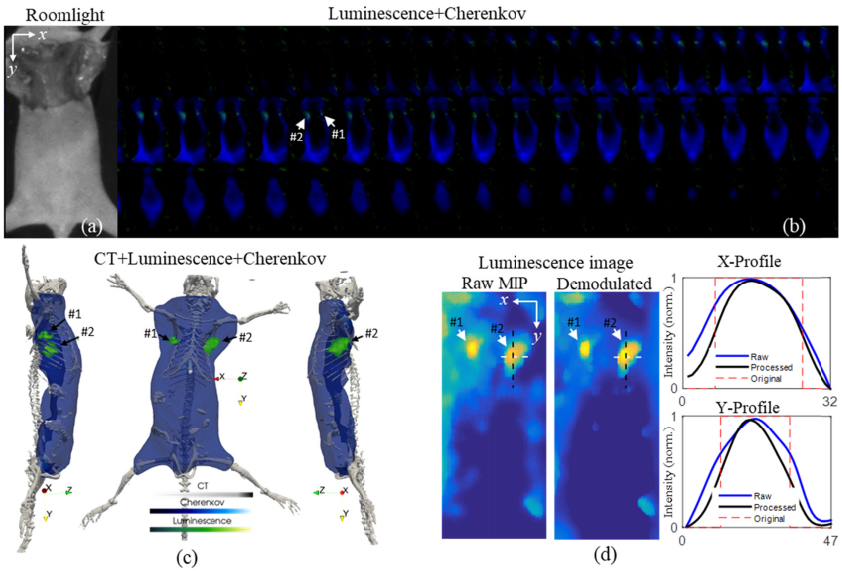

Fig. 12. In-vivo mouse experiment for 3D MDM-CELSI: (a) photograph of nude mouse with one MDA-MB-231 tumor growing on the upper limb flank injected with 50 ml of 25 μM PtG4, (b) merged Cherenkov and demodulated luminescence images, (c) 3D perspective views of combined CT, Cherenkov and luminescence images, and (d) comparisons of luminescence MIP image before and after demodulation and their X-profiles across tumor center. Arrows labeled with #1 and #2 point to the non-tumor and tumor regions, respectively.

5.2 Oxygen sensing with the MDM-CELSI technique

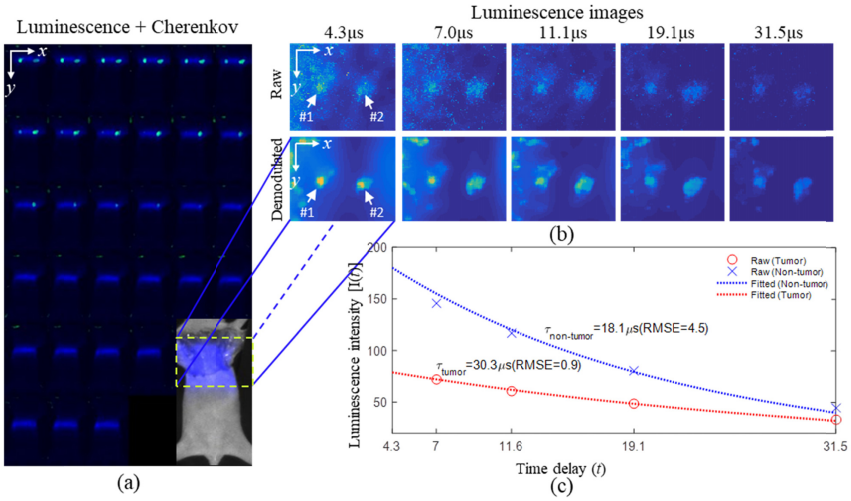

Fig. 13. pO_2 sensing demonstration: (a) merged Cherenkov and demodulated luminescence images, (b) luminescence images of the scanned region before and after demodulation at different post-excitation time points, and (c) raw and fitted luminescence decay cures for the tumor and non-tumor regions. A photograph overlaid with Cherenkov MIP image is shown at the last position of (a). Arrows labeled with #1 and #2 point to the non-tumor and tumor regions, respectively.

To estimate pO_2 concentration reasonably, time-resolved luminescence decay needs to be detected in a limited period. As a result, a localized scanning was performed around the mouse chest region. The transmittance measurements of Cherenkov and demodulated luminescence are shown in Fig. 13(a), where a room light image was overlaid with a

Biomedical Optics EXPRESS

Cherenkov MIP image to indicate the scanning area framed by yellow dashed line. Luminescence images before and after demodulation are shown in upper and lower lines of Fig. 13(b), respectively, for five time delays (t). To pursue high SNR, these measurements were measured as an integration over 100μs with a specified t after Cherenkov period. The curves of luminescence intensity against t [I(t)] for tumor and non-tumor regions were plotted in Fig. 13(c). Curve fitting procedures were performed to achieve a more substantial lifetime (τ), which was calculated according to the following equation:

$$\mathrm{I}(t) = \mathrm{I}_0 \tau \left(e^{-\frac{t}{\tau}} - e^{-\frac{t+100}{\tau}} \right), \tag{2}$$

with I_0 being the decay initial intensity. The estimated τ values for tumor and non-tumor regions were 30.3μs and 18.1μs, with root-mean-square errors (RMSE) being 0.9 and 4.5, respectively. Then pO_2 values were calculated via the Stern-Volmer relationship: 5.6 mmHg and 76.8 mmHg for the tumor and non-tumor regions, respectively. As expected, lower pO_2 was detected for tumor region, which accords with general reports on tumor oxygen level: hypoxic or anoxic [31]. More details can be found in our previous studies on pO_2 tomography with CELSI technique [32,33]. In addition, excitation efficiency of PtG4 proportionally depends on oxygen concentration to some extent, which explains why the intensity in non-tumor region is higher than that in tumor one.

6. Discussion and conclusion

Based on beam scan parameters examined here, and the methodology of post processing the images, a reliable enhancement approach for CELSI imaging is proposed, with an available depth of ~17mm into tissue or tissue-like medium with PtG4-dyed target. By making use of spatial control of the LINAC beam through the programmable MLCs, a modulation of the source (*i.e.*, collimated X-ray) beam could be automatically done, as is typical for radiotherapy regimens today. Phantom experiments showed that a square block pattern generally outperformed the linescan approach, by achieving a similar spatial resolution while providing less radiation dose. The linescan has the potential for faster acquisition but the dose increase can be problematic. Further investigations about these pattern parameters with respect to image fidelity gave a recommended side length of 38mm and beam pitch of 0.33 as specified for the measurement geometry adopted in this paper. From the MTF study results, it is possible to conclude that the spatial resolution at a target depth of 18mm improves from 5.2mm to 1.8mm with the optimized beam parameters. In addition to spatial-resolution enhancement, the proposed strategy was experimentally demonstrated to be capable of out-of-focus deblurring, which could be meaningful for non-contacting imaging modalities.

In most fluorescence imaging modalities, the model-based excitation light fluence-rate is hard to be well predicted with experimentally or empirically estimated optical properties. For CELSI, the excitation source is from X-ray induced Cherenkov photons, which can be captured by the same device for luminescence measurement with a different pulse delay. In this sense, the proposed deconvolution method matches very well with CELSI.

For deeper applications, efforts can be made towards using more optimized oxygen-sensitive probes at lower concentrations [11]. At the same time, scattering-caused blurring by luminescence photons could be compensated with the image deconvolution or reconstruction strategies for diffuse optical imaging [6]. Future work will focus on applying the proposed method to improve depth-resolved CELSI with angled incidence/detection configurations.

Funding

Congressionally Directed Medical Research Program for Breast Cancer Research Program; U.S. Army USAMRAA grant (W81XWH-16-1-0004); National Institutes of Health research grant (R01 EB024498).

Biomedical Optics EXPRESS

Disclosures

The authors declare that there are no conflicts of interest related to this article.